Robotica (2025), **43**, pp. 2693–2709
doi:10.1017/S0263574725101938

CAMBRIDGE UNIVERSITY PRESS

RESEARCH ARTICLE

Configuration-based caging manipulation design for a cable-driven flexible arm with multi self-lockable links

Yufan Zhou, Zhongliang Jing, Jianzhe Huang, Xiangming Dun, Yinshuai Sun and Kai Jiang

School of Aeronautics and Astronautics, Shanghai Jiao Tong University, Shanghai, China
Corresponding author: Zhongliang Jing; Email: zljing@sjtu.edu.cn

Received: 24 January 2025; **Revised:** 29 May 2025; **Accepted:** 5 June 2025; **First published online:** 11 July 2025

Keywords: caging manipulation; caging grasp; manipulation planning

Abstract

In recent years, the removal of orbital debris has become an increasingly urgent task due to advancements in human space exploration. Capturing space debris through caging manipulation offers notable advantages in terms of robustness and controllability. This paper proposes a configuration-based caging manipulation design method for a cable-driven flexible arm. First, the cable-driven flexible arm with multi self-lockable links is introduced. To quantify the caging configurations formed by different self-lockable link selections, a novel planar caging quality metric is then presented for arbitrary planar objects. Using this metric, a caging design method is developed for the flexible arm to conduct caging manipulations. Finally, the caging manipulation strategies are discussed with lock selection maps for different objects, and a robust caging strategy considering uncertainty is further explored. Simulation and experimental results validate the effectiveness of the proposed caging design method and demonstrate better performance compared to conventional caging methods.

1. Introduction

Nowadays, the advancement of human space exploration and exploitation has resulted in a rapid increase in space debris [1]. Addressing the issue of space debris removal has become an urgent problem. Typical collective approaches include the use of soft nets, tethers, and robotic arms [2–4], which are summarized in Table I. Soft nets can adapt to various debris shapes but offer limited controllability, whereas robotic arms provide high controllability but face challenges with debris of different shapes and sizes. Therefore, achieving reliable and robust capture of diverse space debris remains an ongoing challenge.

Recently, caging manipulation has gained increasing interest due to its high compliance. The original concept of caging was introduced by Kuperberg [5] as a problem of finding a formation of planar points that prevents a polygon from moving arbitrarily far from its initial position. This concept has since evolved into a manipulation method for constraining an object's movements, which is initially applied in distributed movable robotics and pin-based grippers [6, 7]. In the context of robotic arms, this concept is similar to envelop grasp [8] and whole-arm grasp [9], where the entire arm is used to close around an object rather than just the end-effectors. Unlike traditional grasp manipulation, which focuses on force control to achieve force closure, caging manipulation primarily focuses on position control to create a cage around the object without considering mechanical properties like contact forces [10]. This approach simplifies robot control and enhances manipulation robustness in the presence of disturbances.

Early works on robotic arm caging manipulation can be traced back to [11]. With the advancement of grasping tasks performed by robotic arms [12–14], caging manipulation has received increasing attention in recent years. In 2019, underactuated robotic hand utilizing caging manipulation was introduced [15]. Bio-inspired soft arms that employ caging strategies have also been developed [16, 17]. Additionally, numerous studies have focused on dexterous grasping manipulation using caging [18, 19].

© The Author(s), 2025. Published by Cambridge University Press.

https://doi.org/10.1017/S0263574725101938 Published online by Cambridge University Press

Table I. *Comparison of space debris capture methods.*

Methods	Advantages	Disadvantages
Robotic Arms	High precision and versatility.	Limited reach and high complexity.
Nets	Effective for irregular debris.	Poor post-capture control.
Tethered Space Robots	Extended reach and maneuverability.	Tether management complexity.
Harpoon	Simple and cost-effective.	Risk of target fragmentation.

While most of these robotic arms form cages using fixed arm parameters, some studies, such as [20–22], propose robotic arms with movable bases to accommodate different objects; However, the caging configuration in these studies is not further explored. In this paper, a cable-driven flexible arm with multi self-lockable links is proposed. The lock devices enable the arm to manipulate in different driving modes, allowing it to form various cages with different configurations. A caging manipulation that utilizes the whole arm for different planar objects has also been presented.

Most previous research utilizes caging as a manipulation method without addressing the design and quality of caging itself. Makapunyo and Makita [23, 24] discuss caging quality mathematically in terms of geometry and escape probability, but they do not consider the characteristics of robotic arm manipulation. Wan [25] explores the caging configuration design of a multi-fingered mechanism, though it remains limited to a fingertip pin-caging approach. Shirizly et al. [26] examine manipulation caging quality using the concept of "basket grasp depth," which accounts for gravity, and [27] introduces a caging quality based on the number of digits wrapping around the object. However, these caging qualities are primarily concerned with gravity, making them unsuitable for space caging scenarios. Raymond proposed a planar caging quality that excludes gravity [28], based on the maximal inscribed circle of the cage, but ignoring the properties with caging objects. Bircher's recent work [29] considers caging with circular objects and quantifies it using the ratio between open finger distance and the circle's radius. However, this quality metric is only applicable to circular objects and does not account for rotational escape.

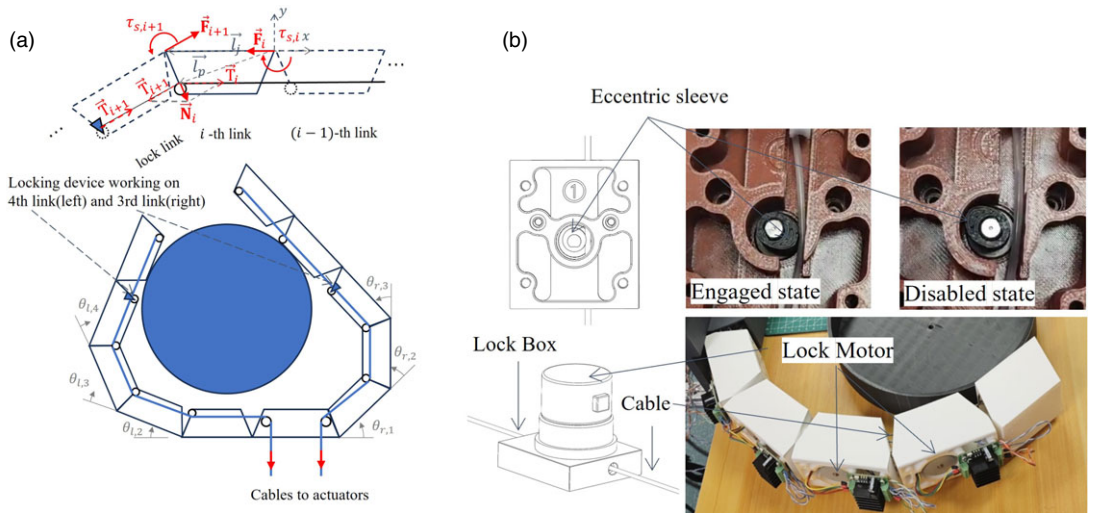
In this paper, a configuration-based caging manipulation design method is proposed for a cable-driven flexible arm with multi self-lockable links. To quantify the caging configurations formed by different self-lockable link selections, a new planar caging quality metric is introduced for arbitrary planar objects, taking into account both rotational and translational escape. A caging manipulation design method is then achieved using the proposed caging quality, which outperforms the conventional caging design cases. Additionally, the caging strategies are discussed for various scenarios based on the simulation and experimental results, and a robust strategy is further explored.

The remainder of the paper is organized as follows: Section 2 introduces the cable-driven flexible arm with multi self-lockable links. Section 3 presents the new planar caging quality and the caging manipulation design method for different objects. Section 4 shows the simulation and experimental results and discusses caging strategies for different situations. Finally, Section 5 presents a brief conclusion and discusses future research directions.

2. Cable-driven flexible arm with multi self-lockable links

To achieve the space debris capture mission, a cable-driven flexible arm is developed with multi self-lockable links, which is shown in Figure. 1. The cable-driven arm is designed with a middle body part and two symmetric arms, each consisting of five links. Instead of employing five motors to drive each link, each arm is actuated by a single cable (depicted as the blue line in Figure. 1a) connected to a linear actuator. Although this design sacrifices some maneuverability, it significantly reduces the weight of the arm, which is crucial for space missions. Each link is equipped with a torsional spring of stiffness K for passive opening. With cable-driven and passive open only, the arm will act in a simple curling mode with only one degree of freedom.

https://doi.org/10.1017/S0263574725101938 Published online by Cambridge University Press



Schematic diagram One arm and lock device details

Figure 1. *Cable-driven flexible arm with multi self-lockable links.*

To enhance the manipulation capabilities, the first four links are designed as self-lockable links installed with lock devices(represented as small circles on the links). Each lock device comprises a lock motor, a lock box, and an eccentric sleeve attached to the lock motor shaft, as shown in Figure. 1b. When the lock device is disengaged, the lock box allows the cable to pass freely. When engaged, the lock motor drives the eccentric sleeve to apply pressure on the cable, constraining it at the engaged link. The driven force is then stopped by the lock device, creating an driven torque to the joint. The general form of the dynamic equation for a single cable-driven arm is expressed as

$$\boldsymbol{M}(\Theta)\ddot{\Theta} + \boldsymbol{C}(\Theta, \dot{\Theta}) + \boldsymbol{D}(\Theta, \dot{\Theta}) = \boldsymbol{\tau} + \boldsymbol{\tau}_{\text{ext}} \tag{1}$$

where $\boldsymbol{M}(\Theta)$ is the mass matrix of the robotic arm, $\boldsymbol{C}(\Theta, \dot{\Theta})$ represents the centrifugal and Coriolis force terms, and $\boldsymbol{D}(\Theta, \dot{\Theta})$ denotes the damping force terms. $\boldsymbol{\tau}$ is the driven torques of each link, and $\boldsymbol{\tau}_{\text{ext}}$ represents torques from external disturbances.

For the cable-driven system depicted in Figure. 1, the driven torque for the i-th link is generated by the cable contact force $\vec{\mathbf{N}}_i$, the link contact forces $\vec{\mathbf{F}}_{i+1}$ and $\vec{\mathbf{F}}_i$ from the subsequent and preceding links, and the torsional spring torques $\tau_{s,i+1}$ and $\tau_{s,i}$ from the subsequent and preceding links. When the lock device is engaged, the link behind the lock link is no longer driven by the cable. Thus, the driven torque τ_i for the i-th link show in Figure. 1a can be given as

$$\tau_i = \vec{l}_{\text{j}} \times \vec{\mathbf{F}}_{i+1} + \vec{l}_{\text{p}} \times \vec{\mathbf{N}}_i + \tau_{s,i+1} - \tau_{s,i}, \quad i = 1, 2 \ldots, lock - 1 \tag{2}$$

where *lock* is the index of the engaged lock device link, $\vec{l}_{\text{j}}$ and $\vec{l}_{\text{p}}$ are link parameter vectors.

Assume that the cable-driven arm is operated in a planar environment without the effects of gravity and the manipulation is quasi-static, meaning it moves slowly enough to ignore inertial effects. By defining the torque from the torsional spring as $\tau_{s,i} = K\theta_i$ and setting the minimum limit angle to 0, substitute (2) into (1) under the quasi-static assumption yields

$$\theta_i = \begin{cases} \theta_{i+1} + \dfrac{\vec{l}_j \times \vec{\mathbf{F}}_{i+1} + \vec{l}_p \times \vec{\mathbf{N}}_i}{K} + \dfrac{\tau_{\text{ext},i}}{K}, & i < \text{lock} \\ \dfrac{\vec{l}_p \times \vec{\mathbf{T}}_i}{K} + \dfrac{\tau_{\text{ext},i}}{K}, & i = \text{lock} \\ 0, & i > \text{lock} \end{cases}, i = 1, 2 \ldots, n \tag{3}$$

https://doi.org/10.1017/S0263574725101938 Published online by Cambridge University Press

where $\tau_{\text{ext},i}$ represents the external disturbances acting on link i, which in the planar case, primarily arise from friction between the arm and the planar platform. $\overrightarrow{\mathbf{T}}_i$ denotes the cable driven force directly applied to the lock link.

Note that for links with $i < lock$, the torque generated by the contact force $\overrightarrow{\mathbf{F}}_{i+1}$ and $\overrightarrow{\mathbf{N}}_i$ act in different directions. In the planar experiment, the external torques generated by friction with the platform are sufficiently large to constrain the motion of the preceding links. Consequently, the cable-driven arm behaves in a curling mode, initiating motion from the lock link and propagate to the preceding links as each link sequentially reaches limit angle. In fact, the torsional spring stiffness K plays a critical role in the arm's behavior, like the backbones do in other flexible arms. With a higher stiffness, the effects of external disturbances $\tau_{\text{ext},i}$ can be minimized with $\theta_i \approx \theta_{i+1} \approx \ldots \approx \theta_{lock}$, but result in a higher cost of cable driven actuator. However, for space environment where the external disturbances are complicated but relatively small, an appropriate higher stiffness will ensure a better arm performance.

The driven mode of the arm is determined at the beginning of the caging manipulation based on the engaged lock devices. For example, when the lock device is engaged on the third link of the right arm (as shown in Figure. 1), the cable is constrained at the third link. As a result, the attitude of the preceding links (1st, 2nd, and 3rd) will change in sequence from the distal link when the right cable drives, while the subsequent links (4th and 5th) remain in their initial zero positions. And this curling movement can be represented by the link altitude Θ as

$$\Theta = \begin{bmatrix} \theta_1 \\ \theta_2 \\ \theta_3 \\ \theta_4 \\ \theta_5 \end{bmatrix} = \begin{bmatrix} 0 \\ 0 \\ \theta_d \\ 0 \\ 0 \end{bmatrix} \xrightarrow{\text{drive}} \begin{bmatrix} 0 \\ \theta_d \\ \theta_{limit} \\ 0 \\ 0 \end{bmatrix} \xrightarrow{\text{drive}} \begin{bmatrix} \theta_d \\ \theta_{limit} \\ \theta_{limit} \\ 0 \\ 0 \end{bmatrix}, \text{lock} = 3 \tag{4}$$

where θ_d is the driven angle, and θ_{limit} is the joint limit angle.

Consequently, the arm operates as a single-degree-of-freedom curling mechanism, where joints actuated by the cable move sequentially from the distal link. Since the left and right arms are driven by separate cables, different selections for each arm can result in an asymmetric configuration. Note that the cable is always fixed at the fifth joint, "locking the i-th link" refers to the nearest locking link number to the body. As a matter of fact, the subsequent lock devices do not affect the arm's configuration. Using the arm configuration form derived in (4) for different lock links, the caging quality and lock device planning are then discussed in the following sections.

3. Configuration-based caging design method

In this section, the caging manipulation design method is introduced based on the configurations formed with different planar caging cases. Using different lock device selections, various contacting configurations can be achieved by the cable-driven arm. A caging quality for planar objects is then proposed to evaluate the caging manipulation with different caging configurations. Using this metric, the caging manipulation design is completed for various situations using different lock device selections.

3.1. Planar caging quality

After the caging is achieved, the caging quality is then used to evaluate the object's ability to escape from the cage. The prior work in [29] introduced a simple caging quality metric for circular objects, defined as the ratio between the circle diameter and the opening distance. To generalize this metric for arbitrary planar objects, the circle diameter has been extended to the maximum projected in-arm object length onto the opening, as illustrated in Figure. 2, and are calculated with the definitions in equation (6) and (8). It is important to note that these extended lengths are not intrinsic properties of the object, but should be calculated based on the different caging configurations formed by both the arm and the object.

https://doi.org/10.1017/S0263574725101938 Published online by Cambridge University Press

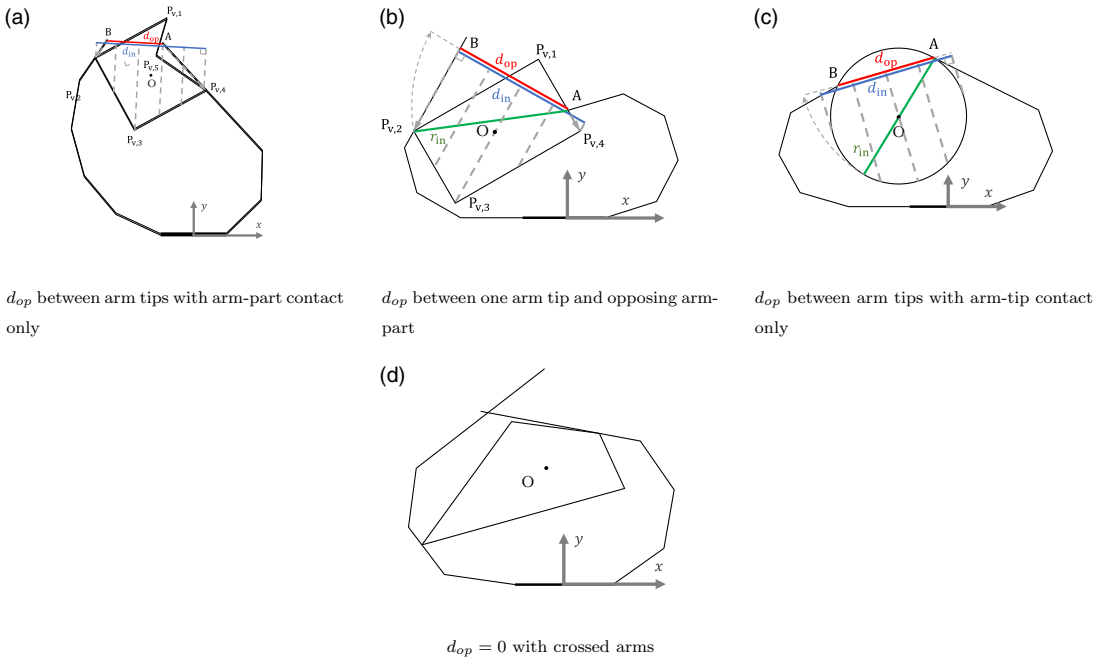


Figure 2. *Planar caging scenarios for a dual-arm robot.*

For the translational escape scenario, the ability to escape is quantified by computing the translational escape ratio γ_t, which is the ratio of the opening arm distance d_{op} between the arms (where translational escape could occur) to the maximum object in-arm characteristic length d_{in}, which prevents the escape. According to this ratio, only a translational escape ratio less than 1 is considered an effective translation cage, while a cage with a translational escape ratio of 0 is the most effective, without any opening for escape.

$$\gamma_t = \frac{d_{op}}{d_{in}} \in [0, 1] \tag{5}$$

The definition of the opening arm distance d_{op} is similar to the opening finger distance defined in [29], which is the minimum distance between arm tip and the opposing arm. In the cable-driven robotic arm case, this minimum distance can be found as either the distance between the arm tips(Figure. 2a and 2c), the normal distance from one arm tip to an opposing arm(Figure. 2b), or zero if there is no opening for the object to escape through translation (Figure. 2d). Various scenarios for opening arm distance d_{op} are shown in Figure. 2 as the red line. The two points used to calculate d_{op} are labeled as "A" (for the first arm tip if arm-tip contact exists) and "B". The vertices on the object boundaries are labeled as "$P_{v,1}, P_{v,2} \ldots, P_{v,n}$".

The characteristic length d_{in} is defined as the maximum projection length of the in-arm object part onto the arm opening, as illustrated by the blue line in Figure. 2. When the arm contacts the object with link body, it is referred to as "arm-part contact," in which case the object's translation is restricted by the arm part. The object in-arm diameter d_{in} is then calculated as the sum of the opening distance d_{op} and the exceeding object part projected to the opening (Figure. 2a and 2b). When both arms contact the object with tips, the object can translate freely along the object's edge, d_{in} is then calculated as the object's maximum cross-sectional length parallel to the opening (Figure. 2c).

$$d_{in} = \begin{cases} \max\limits_i \left(\dfrac{\overrightarrow{AB} \cdot \overrightarrow{BP}_i}{|\overrightarrow{AB}|}, 0 \right) + \max\limits_i \left(\dfrac{\overrightarrow{BA} \cdot \overrightarrow{AP}_i}{|\overrightarrow{BA}|}, 0 \right) + |\overrightarrow{AB}|, & \textit{if arm-part contact exists} \\ \max\limits_i \left(|\overrightarrow{P_iP'_i}|, |\overrightarrow{AB}| \right) \quad \text{with} \quad \overrightarrow{P_iP'_i} \parallel \overrightarrow{AB}, & \textit{if no arm-part contact exists} \end{cases} , P_i \in \mathbf{P}_{ob,in} \tag{6}$$

https://doi.org/10.1017/S0263574725101938 Published online by Cambridge University Press

where $P_i, P_i' \in \mathbf{P}_{ob,in}$ represent the points on the object boundary inside the opening AB.

Rotational escape is considered only when "arm-tip contact" exists, since the outside arm part will always prevents the object from free rotation in the "arm-part contact" case. Examples of these rotational escape scenarios are demonstrated in Figure. 2b and 2c. When "arm-tip contact" occurs, the rotational escape ratio γ_r is defined as the ratio between the opening arm distance d_{op} and the maximum in-arm rotation radius r_{in}.

$$\gamma_r = \frac{d_{op}}{r_{in}} \in [0, 1] \tag{7}$$

The characteristic length r_{in} is defined as the maximum length between the in-hand object part to the rotation center (chosen as the contacted arm tip). When there are two arm-tip contacts, as shown in Figure. 2c, the in-arm rotation radius is chosen as the smaller one to represent the ability of rotational escape. When this radius is larger than the opening arm distance, the opposing arm will prevent the object from free rotation around the tip. Therefore, an "arm-tip contact case" with a rotational escape ratio no larger than 1 is considered an effective rotation cage. For computation convenience, the rotational escape ratio is set to 0 for "arm-part contact" cases and 1 for ineffective cases where d_{op} is larger than r_{in}. The in-arm rotation radius r_{in} can be calculated by

$$r_{in} = \begin{cases} \max\limits_i (|\overrightarrow{AP}_i|, |\overrightarrow{AB}|), & \textit{if} \text{ only one arm-tip contact exists} \\ \min\left(\max\limits_i (|\overrightarrow{AP}_i|, |\overrightarrow{AB}|), \max\limits_i (|\overrightarrow{BP}_i|, |\overrightarrow{BA}|), \right. & \left. \textit{if} \text{ two arm-tip contact exist.} \right. \end{cases}, P_i \in \mathbf{P}_{ob,in} \tag{8}$$

With the definition of characteristic lengths d_{in} and r_{in}, the geometric escape ratio has been generalized to arbitrarily planar shapes. It should be noted that, these characteristic lengths return to the circle diameter in the case of caging circular objects, as shown in Figure. 2b, thereby aligning with the prior work in [29]. Considering both translation and rotation, the overall caging quality c_q is defined as follows. For ineffective caging where $\gamma_t = 1$ or $\gamma_r = 1$, the caging quality c_q is zero.

$$c_q = (1 - \gamma_t)(1 - \gamma_r) \in [0, 1]. \tag{9}$$

This term quantifies the caging score of a given object-arm configuration, with a higher score indicating a more effective caging manipulation. This caging quality is then used to determine the most effective caging in the next section.

3.2. Caging manipulation design

For a given object, the optimization of the engaged lock devices is conducted based on the caging quality metric at the moment of initial contact. By varying the engaged lock devices, the motion mode of the arm changes and result in different arm models. Consider the motion of object, the object could be at different positions and orientations when contact occurs. These contact configurations generated by combining the arm and object models are simulated to compute the corresponding caging quality, which is then used to optimize the caging manipulation strategy. This section details the caging manipulation design simulation for various planar objects, with the pseudocode for the simulation presented in Table II.

The caging manipulation design is simulated across a grid of object position points in front of the arm. Due to the symmetric design of the cable-driven arm, the grid points need to cover only half of the area in front of the middle body. After simulating the left half area, the results for the right half can be mirrored. To generate planar object models with different shapes, the object model is defined as $\mathbf{P}_{ob}$. For planar polygons with n vertices, the object model can be represented by its vertices as

$$\mathbf{P}_{ob} \in \mathbb{R}^{2\times n} = (P_{v,1}, P_{v,2}, \ldots, P_{v,n}) \tag{10}$$

where $P_{v,i} \in \mathbb{R}^{2\times 1}$ is the position vector of the i-th vertex on the polygon.

Once the object center "O" is determined (chosen as the geometric center or rotation center), the vertices of the polygon can be determined in the following format. The examples for different polygon

https://doi.org/10.1017/S0263574725101938 Published online by Cambridge University Press

Table II. *Caging manipulation design peso code.*

Input object parameters size, $\boldsymbol{r}$, $\boldsymbol{\phi}$
Input arm parameters and simulation parameters
for object position $(x_{oc}, y_{oc}) = (x_s, y_s)$ **to** (x_e, y_e)
  for object orientation $\alpha_{oc} = \alpha_s$ **to** α_e
    generate object model $\mathbf{P}_{ob}$ using (10) and (11)
    for lock device selection $(s_1, s_2) = (2, 2)$ **to** $(5, 5)$
      for arm number $k = 1, 2$
        for $i = s_k$ **to** 1
          for $\theta_i = 0$ **to** θ_{limit}
            generate arm model $\mathbf{P}^k_{arm}$
            if contact $(\mathbf{P}_{ob}, \mathbf{P}^k_{arm}) =$ **true then break**
    $\mathbf{P}^l_{arm} \leftarrow \mathbf{P}^1_{arm}$, $\mathbf{P}^r_{arm} \leftarrow \mathbf{P}^2_{arm}$,
    get d_{op} and opening point A, B using arm model
    calculate d_{in}, r_{in} using (6) and (8)
    compute γ_t and γ_r using (5) and (7)
    compute and save the caging quality $c_q(s_1, s_2, \alpha_{oc})$ using (9)
  $(s_1, s_2)_{best} \leftarrow \text{argmax}_{s_1,s_2}(\Sigma_{\alpha_{oc}} c_q(s_1, s_2, \alpha_{oc}))$
plot selection map using $(s_1, s_2)_{best}$ at (x_{oc}, y_{oc}) for orientation α_{oc}

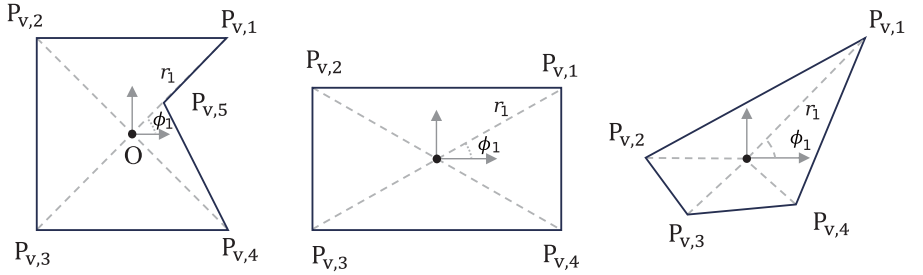


Figure 3. *Polygon objects defined with different shapes.*

shapes simulated in this paper can be find in Figure. 3.

$$\mathrm{P}_{v,i} = p_{oc} + \text{size} \cdot r_i \cdot \begin{bmatrix} cos(\phi_i + \alpha_{oc}) \\ sin(\phi_i + \alpha_{oc}) \end{bmatrix}, i = 1, 2, \ldots, n \tag{11}$$

where $p_{oc} \equiv (x_{oc}, y_{oc})^T \in \mathbb{R}^{2\times 1}$ and α_{oc} are the object center position and orientation given by the simulation separately. size, $r_i \in \boldsymbol{r}$, and $\phi_i \in \boldsymbol{\phi}$ are the given object parameters determining the polygon shape with n vertices.

With the given object parameters $\boldsymbol{r}$ and $\boldsymbol{\phi}$, the polygon object model $\mathbf{P}_{ob}$ at position p_{oc} and orientation α_{oc} can be generated. For different engaged lock device selections s_1 and s_2 for left arm and right arm separately, the arm model $\mathbf{P}_{arm}$ contacts with object can be simulated with an ever-increasing joint angle. After getting the contact model consisting of the arm and object, the caging quality of this model is then calculated using the defined translational escape ratio and rotational escape ratio. The best lock device selection is plotted for different orientations at each simulation grid point (x_{oc}, y_{oc}).

The object parameters for different shapes simulated in this paper are provided in Table III. It should be noted that, for other object shapes like circles, the object model $\mathbf{P}_{ob}$ can be directly represented by the boundary equation as $\mathbf{P}_{ob} \equiv \{p = (x, y)^T | (x - x_{oc})^2 + (y - y_{oc})^2 = \text{size}^2\}$, so the circular object parameters are represented by the radius r only.

The geometry parameters of cable-driven arm used for simulation are given in Table IV. Based on the work space, the simulation area parameters are chosen as $x_s = 0$ mm, $y_s = 100$ mm, $x_e = -200$ mm,

https://doi.org/10.1017/S0263574725101938 Published online by Cambridge University Press

Table III. *Object parameters.*

Object Shape	Shape parameters
Circle	size = 90, 105, 120(*mm*);
Concave polygon	size = 100(*mm*); $\boldsymbol{r} = [1.2;1.2;1.2;1.2;0.4]$, $\boldsymbol{\phi} = [\frac{\pi}{4};\frac{3\pi}{4};\frac{5\pi}{4};\frac{7\pi}{4};\frac{\pi}{4}]$
Rectangle	size = 100(*mm*); $\boldsymbol{r} = [1.2;1.2;1.2;1.2]$; $\boldsymbol{\phi} = [\frac{\pi}{6};\frac{5\pi}{6};\frac{7\pi}{6};\frac{11\pi}{6}]$
Convex polygon	size = 100(*mm*); $\boldsymbol{r} = [1.6;0.96;0.77;0.64]$; $\boldsymbol{\phi} = [\frac{\pi}{4};\pi;\frac{5\pi}{4};\frac{7\pi}{4}]$

Table IV. *Geometric parameters of arm.*

Trapezoid middle body part		Trapezoid link part		Parallelogram link part	All parts	
Shorter length	Longer length	Shorter length	Longer length	Upper length	Heighth	Limit angle
93 mm	126 mm	67 mm	100 mm	84 mm	55 mm	$\pi/4$

$y_e = 300$ mm to simulate a square area in front of the arm, and orientation range is chosen as $\alpha_s = 0$, $\alpha_e = 2\pi$ for robust simulation selection map with orientation uncertainty. The resolution for the position grid and orientation are $x_r = y_r = 5$ mm and $\alpha_r = 0.1$ rad, respectively.

4. Simulation and experimental results

Using the proposed caging design simulation, the most effective caging configurations are achieved at each simulated points for all lock device selections. This section discusses the caging manipulation design results for different object sizes and shapes using selection maps and caging qualities. Additionally, for objects with uncertainties in orientations and sizes, a robust selection map is provided by optimizing the average caging quality across all possible orientations and sizes.

4.1. Experimental setup

The experimental platform is shown in Figure. 4, which comprises a dual-arm robot and an electric linear actuator. The flexible arms are individually connected to two linear actuators via cables. Position control is implemented on the control panel of linear actuators to drive the flexible arm. Each arm is designed with isosceles trapezoidal links with a limit angle of $\frac{\pi}{4}$, while the fifth link is a parallelogram. Additionally, the first four links are equipped with lock devices, each independently controlled by a stepper motor through the control panel.

To implement planar experiment, the cable-driven robotic arm is placed on a horizontal plane. Some important geometric parameters of the cable-driven robotic arm are listed in Table IV. Experiments on several cases with typical caging configurations are conducted to validate the effectiveness of the caging design method. During the experiments, planar objects are first positioned and oriented on a graph paper. In the dynamic experiment, the object center O is connected to an additional rotating motor fixed on the desk, with a clockwise rotational speed around 30°/s. Next, the lock devices are engaged based on the simulated selection map. Finally, the electric linear actuator drives the arm to the position where contact with the objects occurred. The experimental results are presented in the following section as time series from I to V. The results demonstrate that the caging configurations generated using the proposed design method are consistent with the simulations. Some experimental errors may arise from the setup between links and cable-driven errors.

4.2. Caging design for different sizes and shapes

The caging planning results are illustrated as colored maps, depicting lock device selections under different cases. In the lock device selection maps, the colored regions marked with number pairs represent

https://doi.org/10.1017/S0263574725101938 Published online by Cambridge University Press

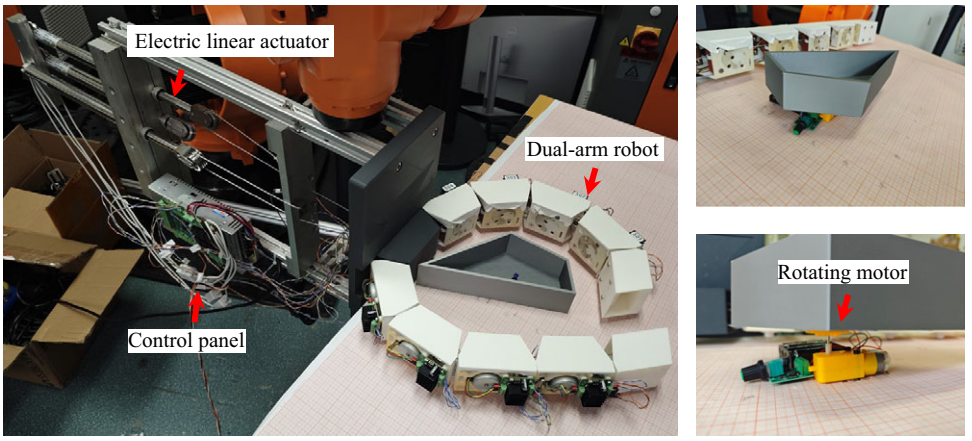


Figure 4. *Experiment platform.*

planned selections for different object positions. Small orange circles denote areas with multiple optimal lock device selections, while gray circles represent ineffective areas where caging fails. For example, the "4-3" area in Figure. 5b denotes that the best caging quality in this area is achieved by engaging the 4th and 3rd lock devices on the left and right arms, respectively.

The caging manipulation is first analyzed for circular objects of various sizes. The simulated lock device selection maps and experimental results for caging circles of different sizes are presented in Figure. 5. From Figure. 5a, four distinct lock device selection areas can be observed. When the object is positioned near the symmetry axis of the middle body, which is $x = 0$ in the diagram, the optimal lock device selections is "3-3," which is also symmetric. As the object moves to the left side, the optimal selection gradually changes to "4-3," "4-4," and finally "5-4". When the circular object is positioned on the left side in front of the arm, the lock number on the left arm is consistently greater than that on the right arm. The selection maps in Figure. 5b and 5c with larger sizes are also consistent with this pattern. This suggests that the left arm should be configured in a relaxed mode, allowing more links to adapt to the object's shape, while the opposing arm should be set in a stiff mode, with a longer distal section to enclose the object.

As the object size increases in Figure. 5b, the "4-3" area gradually occupies more of "3-3" area. This suggests that the relaxed arm strategy becomes more effective for larger objects. However, when the object size becomes sufficiently large, as shown in Figure. 5c, the full relaxed arms like "5-5" and "5-4" may lose effectiveness due to the limited curling working height.

Besides different sizes of circle, caging for different shapes is also investigated. The selection maps for various shapes, including concave polygons, rectangles, and convex polygons, are presented in Figure. 6. The results clearly show that the selection map varies with the object's shape. Compared to the rectangle object case, the concave object case exhibits a higher area of "3-3" due to its concave geometry. In the convex polygon case, when the object has a sharp geometry, as shown in Figure. 6c, the "3-2" lock device selections appears in the top area. This indicates that for objects with sharp, thin shapes in specific orientations, the stiff caging strategy can be more effective than the relaxed caging strategy.

To demonstrate the improved caging performance achieved with the designed lock device selection maps, caging quality cloud maps for the proposed manipulation are presented in Figs. 7 and 8. The caging quality for each simulation area is visualized using a color gradient, with values ranging from 0 to 1. Areas with perfect caging ($c_q = 1$) are depicted in red, while ineffective caging areas ($c_q = 0$) are shown in gray. Since the design method is based on the self-lockable links, the compared conventional caging cases are chosen as fixed link layouts chosen as "3-3," "4-4," and "4-3" link configurations. The overall average caging quality for the simulated square region, denoted as $C_{q,avg}$, is calculated to represent the whole working region's caging score. The effective caging area in percentage to the simulation area is also calculated as A_{eff}, which is used to compare the effectiveness in Table V.

https://doi.org/10.1017/S0263574725101938 Published online by Cambridge University Press

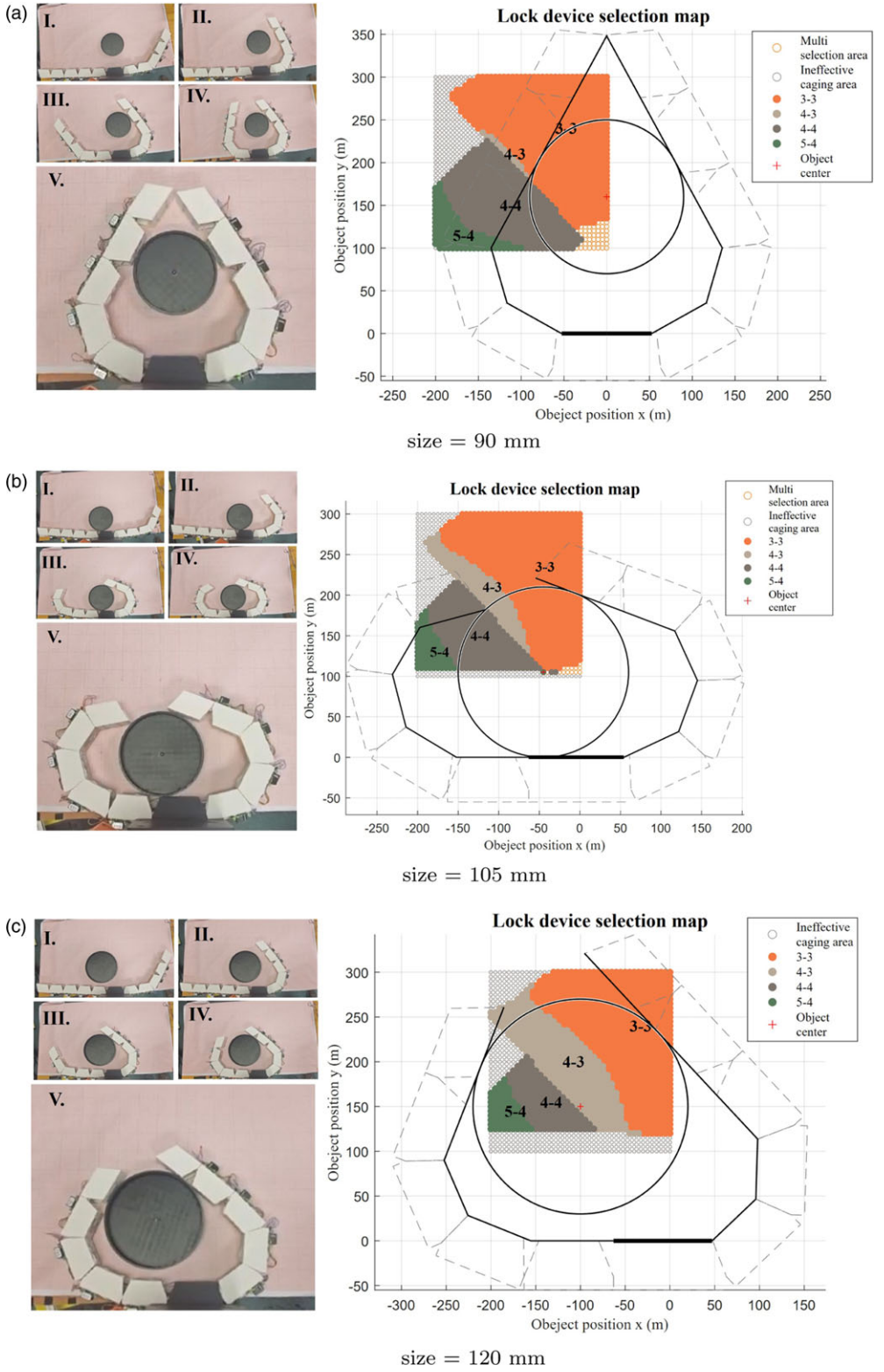


Figure 5. *Selection map for different circle sizes.*

https://doi.org/10.1017/S0263574725101938 Published online by Cambridge University Press

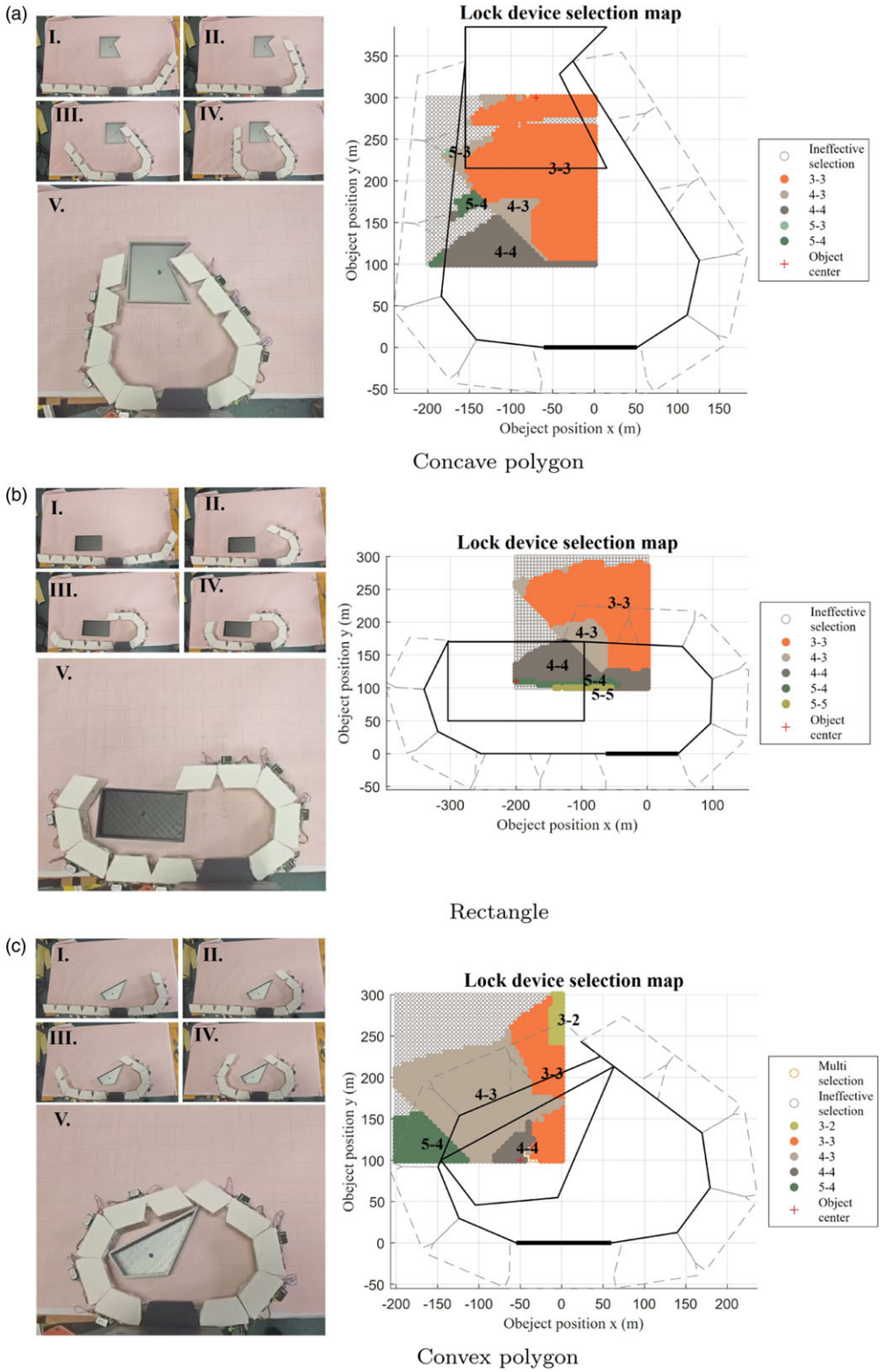


Figure 6. *Selection map for different object shapes.*

https://doi.org/10.1017/S0263574725101938 Published online by Cambridge University Press

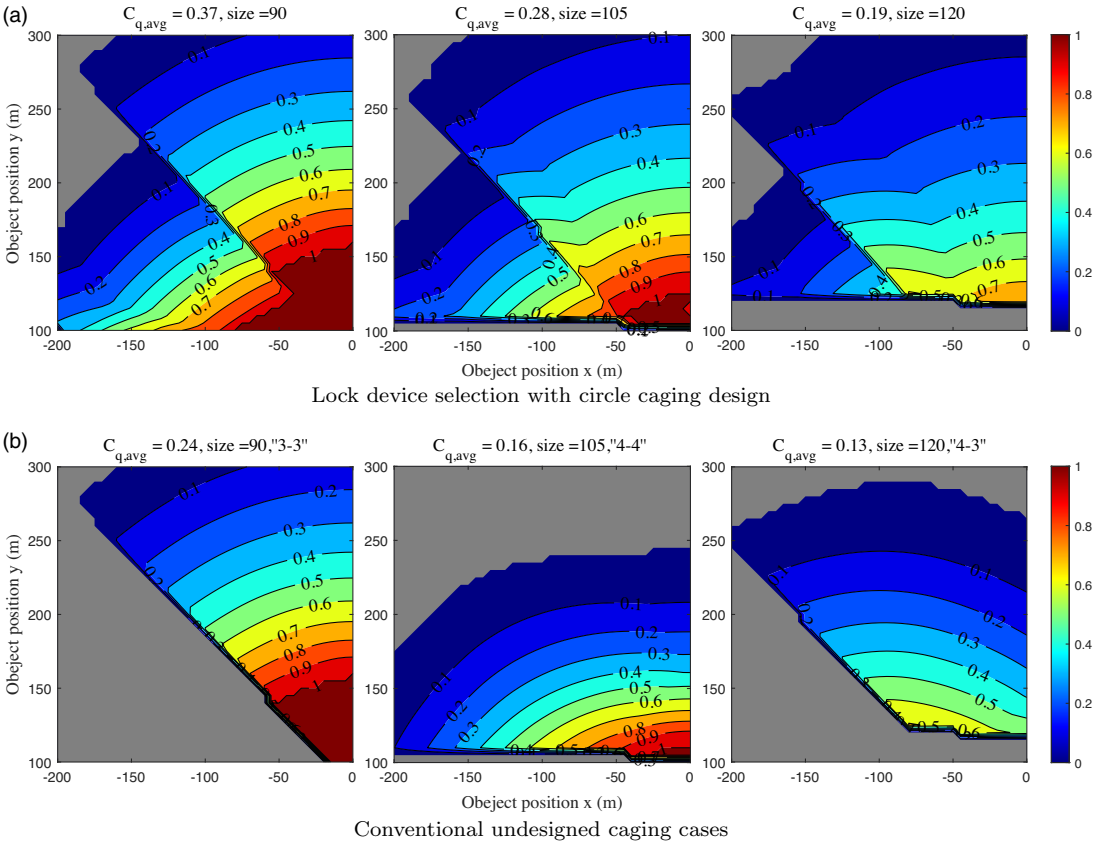


Figure 7. *Caging quality comparison for different circle sizes.*

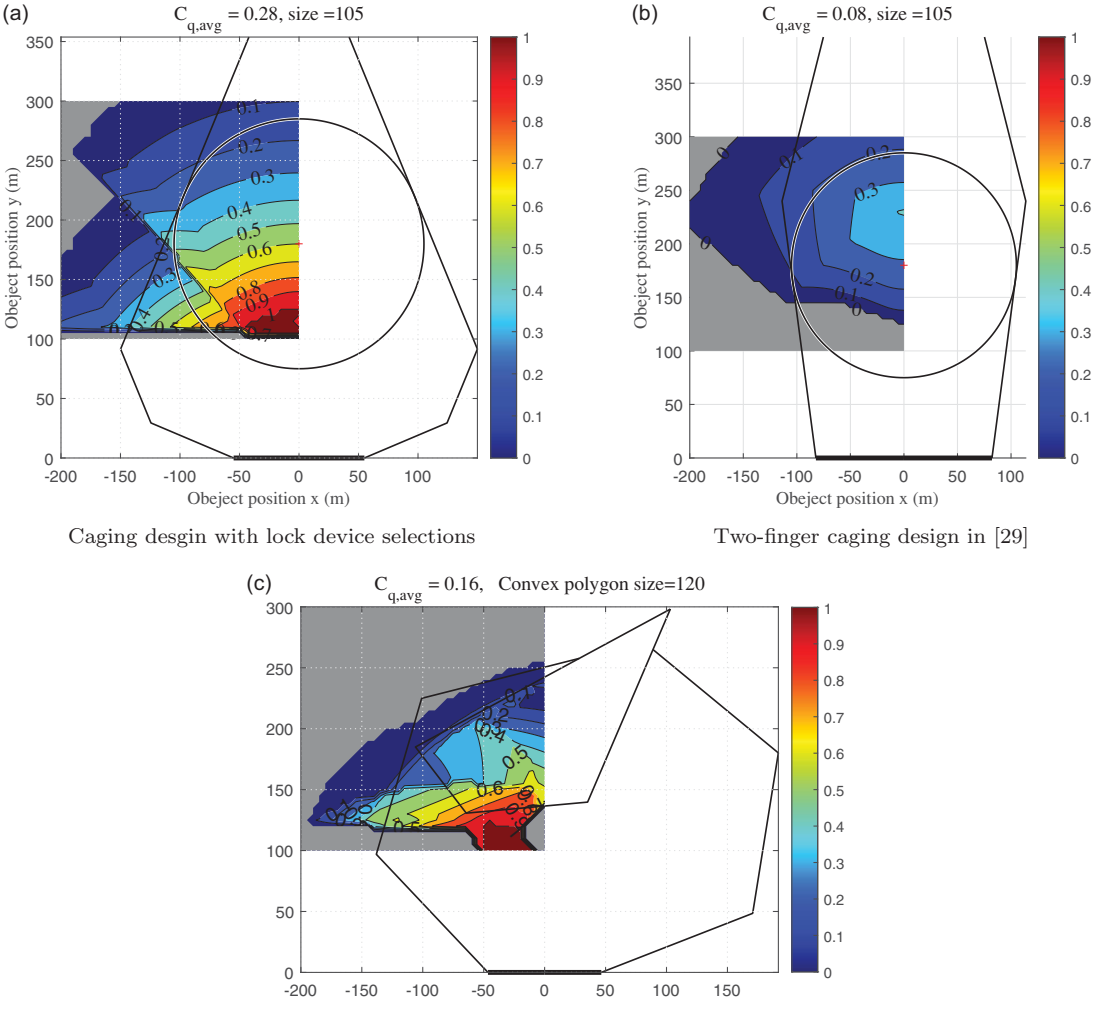
Figure 7 shows the caging quality map for circular objects with different sizes. The cloud map demonstrates that caging quality improves as the object's position approaches the middle body part. The effective area remains relatively stable for object positions far from the body, as the increased size partially facilitates contact with the object. However, as the object size increases, ineffective caging areas expand near the x axis. This phenomenon occurs because, when the circle's radius reaches 105 mm and 120 mm, objects in regions where $y < 105$ mm and $y < 120$ mm penetrate the middle body part. Another notable observation from the cloud map is the rapid change in caging quality near a diagonal line. This behavior arises due to the link's angle being limited at $\frac{\pi}{4}$, suggesting that objects should be approached along paths that avoid this diagonal line. Furthermore, the perfect caging area of the designed case coincides with the multi-selection area in the selection map near the middle body part, indicating a higher redundancy within the perfect caging area.

The comparison with different caging design methods is shown in Figure. 8. Two methods from the literature are chosen for comparison: the two-finger caging design in [29] and the three-link caging using the "One way distance" method in [25]. In the two-finger caging design case, the parameters for the proximal link, distal link, and palm width are selected as the best design parameters, and scaled up to a full arm length of 400 mm for comparison. The lengths of the links and palm are given as: $l_{\mathrm{p}} = 0.604 * 400\ \mathrm{mm} = 241.6\ \mathrm{mm}$, $l_{\mathrm{d}} = 0.395 * 400\ \mathrm{mm} = 158\ \mathrm{mm}$, and $p_{\mathrm{w}} = 0.411 * 400\ \mathrm{mm} = 164.4\ \mathrm{mm}$. For the three-link caging model using the "One way distance" method, the four-fingered mechanism is simplified to a dual-finger model for planar comparison, and the three-link model is used as a one DOF curling model. The link length and palm width are chosen as $l_{\mathrm{link}} = 400/3\ \mathrm{mm} = 133.33\ \mathrm{mm}$ and $p_{\mathrm{w}} = 93$ mm to match the comparison case. The circle and concave polygon cases are omitted, as the "One way distance" method is only applicable to convex polygon cases. To employ the "One way

https://doi.org/10.1017/S0263574725101938 Published online by Cambridge University Press

Table V. *Comparison with caging design methods in literature.*

Object cases	**Circle r = 105 mm**		**Concave polygon**		**Rectangle case**		**Convex polygon**	
Criteria	$C_{q,avg}$	A_{eff}	$C_{q,avg}$	A_{eff}	$C_{q,avg}$	A_{eff}	$C_{q,avg}$	A_{eff}
Proposed method using locking device selection	**0.28**	**86.6%**	**0.22**	**73.7%**	**0.26**	**77.5%**	**0.24**	72.1%
Two-finger model using caging design in [29]	0.08	74.0%	0.07	60.3%	0.06	72.6%	0.08	**74.9%**
Three-link curling model using 'One Way Distance' in [25]	—	—	—	—	0.08	19.6%	0.16	52.2%



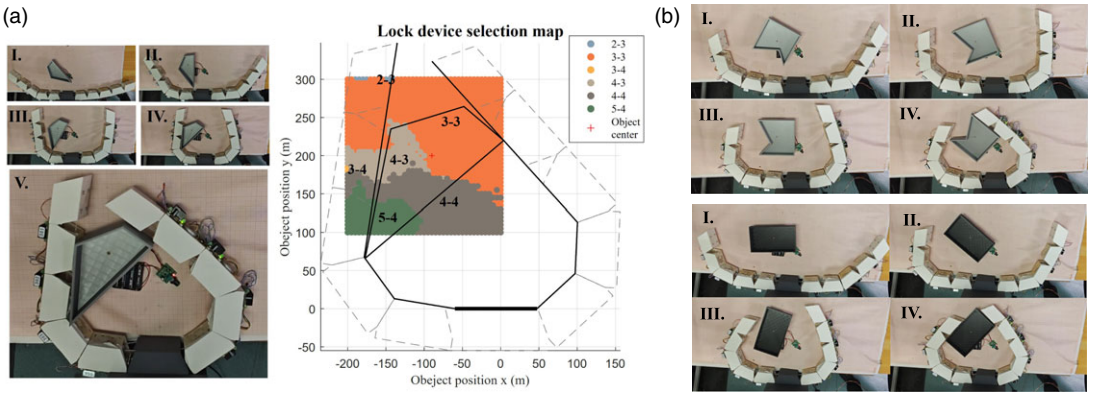
Caging desgin with lock device selections

Two-finger caging design in [29]

Three-link curling model using 'One Way Distance' in [25]

Figure 8. *Caging quality comparison for different caging design methods.*

https://doi.org/10.1017/S0263574725101938 Published online by Cambridge University Press



Robust selection map considering orientation uncertainties

Rotating caging cases for concave and rectangle objects

Figure 9. *Robust caging with rotating objects.*

distance" method, the object caging edges are chosen as $P_{v,2}P_{v,3}$, $P_{v,1}P_{v,4}$ for the rectangle case, and $P_{v,1}P_{v,2}$, $P_{v,1}P_{v,4}$ for the convex polygon case. The criteria are chosen as $C_{q,avg}$ and A_{eff} to compare the caging quality and effectiveness. The results are summarized in Table V.

From the comparison in Table V, it can be observed that the Two-finger caging design achieves a sufficiently close effective caging area A_{eff} compared to the proposed design, and even surpasses it in the convex polygon case. This coincides with the stiff caging strategy using two links mentioned before. This is benefited by the focus on the proximal and distal link parameters, but is still outperformed by the proposed design method which can change the link layouts with different lock devices selections. With the discussion on planar caging quality and lock device selections, the proposed caging design method demonstrates a significant advantage over conventional caging design methods.

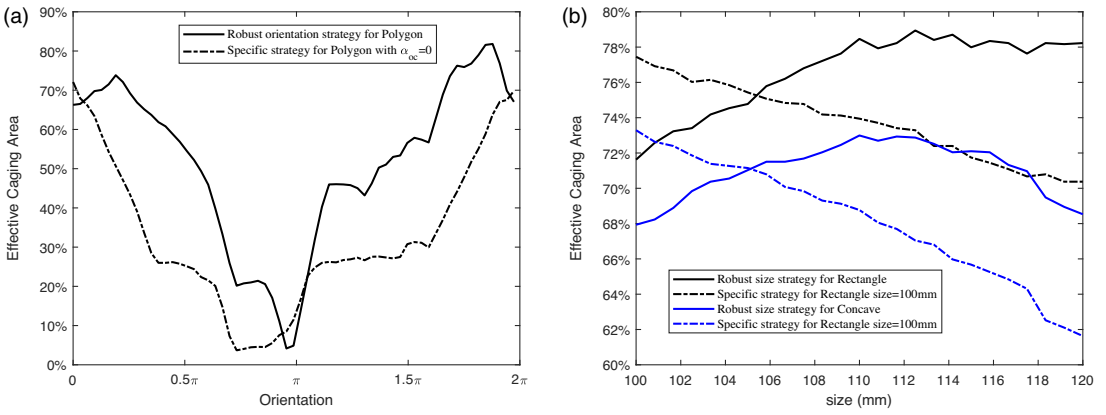
4.3. Robust caging manipulation strategy

In the previous section, the caging manipulation design with optimize caging quality is discussed for specific object information. The selection maps presented above provide optimal caging manipulation configurations based on the object's specific information. However, uncertainties may arise due to variations in object motion and shape. To address these uncertainties, a robust caging manipulation strategy is developed by replacing specific information with a range of possible values.

For the uncertainties arising from motion, the lock device could be planned within a range of possible positions and orientations where the object may be located when contact occurs. The former can be achieved by increasing the resolution of the simulated grid points. To address orientation uncertainties, the robust selection map is developed by averaging the caging quality over an orientation ranges from α_s to α_e for each simulated point. By selecting the configuration with the highest average quality within the orientation range, this robust selection map is more resistant to orientation disturbances. Using the convex polygon as an example, the robust selection maps for orientation ranges from 0 to 2π are presented in Figure. 9.

A dynamic caging experiment with rotating object was conducted using the robust caging selection map considering orientation uncertainties, as shown in Figure. 9a. The experimental results are presented as time series from I to V, showing the caging process with a clockwise rotating object. The results demonstrate that the arm can successfully cage the object using the planned robust caging strategy. Compared to the specific strategy for orientation $\alpha_{oc} = 0$ in Figure. 6c, the "3-2" area in the robust strategy has changed into "3-3," with a significantly larger "3-3" area on the left side. This suggests that stiff configurations perform more effectively under orientation uncertainties, particularly for remote

https://doi.org/10.1017/S0263574725101938 Published online by Cambridge University Press



Effective Caging Area for different orientations Effective Caging Area for different sizes

Figure 10. *Comparison between Robust caging strategies and specific strategies.*

caging manipulations. Other rotating caging experiments are also shown in Figure. 10b, demonstrating the effectiveness of the proposed configuration planning method.

To clearly demonstrate the advantages of the robust caging strategy, the effective caging area A_{eff} is compared with the specific strategy for the convex polygon case in Figure. 10a. Since A_{eff} represents the percentage of the effective caging area within the simulated region, the results demonstrate that the robust strategy achieves a larger effective area for most orientations, whereas the specific strategy performs better only within a narrow orientation range near $\alpha_{\text{oc}} = 0$ and π.

For uncertainties arising from object shape sizes, the robust selection map could be adapted to accommodate a range of possible sizes. Figure 10b compares the robust strategy for sizes ranging from 100 to 120 mm with the specific strategy for size = 100 mm. The result shows that the effective areas of the specific strategy decrease for both rectangular and concave shapes as the object size increases. In contrast, the robust strategy maintains a relatively larger effective area. This is attributed to the increased size enabling the arm to contact objects in regions far from the arm, thereby expanding the effective caging area. A similar trend can be observed in circular caging cases with different sizes in Figure. 8a. Similar to the comparison of orientations, the robust strategy outperforms the specific map across most size ranges, while being surpassed near the specific size, which is a sacrifice made to achieve better overall performance. In essence, the robust strategy considering uncertainties can be regarded as a composite of various specific selection maps. Considering this property, the robust caging strategy can be flexibly generated by combining different selection maps in practical use.

5. Conclusion

In this paper, a caging manipulation design method is proposed for a newly developed flexible arm with multi self-lockable links. A novel planar caging quality metric considering translational and rotational escape is introduced for arbitrary objects. Based on the proposed caging quality, caging manipulation is designed by providing an optimal lock device selection map for different objects.

To demonstrate the advantages of the proposed caging design method, average caging quality $C_{\text{q,avg}}$ and effective caging area percentage A_{eff} are compared with other caging design methods mentioned in literature. The results show that the designed caging manipulation offers advantages over conventional cases, due to the optimization of planar caging quality and variation in link layouts with lock device selections. The planar experiments further validate the effectiveness of the caging configurations generated with multi self-lockable links using selection maps. The method presented here can be applied to various planar capture scenarios with different arm models, once provide the contact configuration between the arms and objects.

https://doi.org/10.1017/S0263574725101938 Published online by Cambridge University Press

The selection maps for caging different objects also provide effective caging strategies for various objects in different positions. For instance, a relaxed arm-fitting strategy is suitable for large objects near the symmetry axis, while a stiffened arm-closing strategy is more appropriate for thin and sharp objects. Furthermore, a robust strategy considering object uncertainty is developed, based on the average caging quality across a range of uncertainties. This robust strategy can be viewed as a composite of multiple specific selection maps, indicating that the proposed selection maps for caging manipulation planning can be adapted to address other uncertainties.

As a matter of fact, the proposed planning method relies on object information to generate contact configurations. For objects with specific information, the specific caging selection map provides optimal caging. For cases considering object uncertainties, the robust caging strategy offers suboptimal caging for sacrifice to achieve better overall performance, but may still fail if the object's information significantly deviates from the considered range. For future research, lock device selection control with attitude feedback, rather than pre-determined selections, will be studied to provide more effective caging manipulations with object uncertainties. Furthermore, planar caging with two arms may be extended into 3D caging scenarios involving more arms. Such cases could introduce greater complexity due to potential escapes through gaps between arms, and the increased computational burden of managing more arms in a three-dimensional space could also pose a significant challenge.

Authors' contributions. Yufan Zhou: Conceptualization, methodology, experiment, writing – original draft; Zhongliang Jing: supervision, writing – review & editing; Jianzhe Huang: writing – review & editing; Xiangming Dun: writing – review & editing; Yinshuai Sun: experiment, writing – review & editing; Kai Jiang: experiment.

Financial support. This work was partially supported by the National Natural Science Foundation of China (Grant No. 61673262), National Basic Research Program under JCKY2021110B134, and the Fundamental Research Funds for the Central Universities, Engineering Research Center of Aerospace Science and Technology, Ministry of Education.

Availability of data and material funding. All data, models, and code generated or used during the study appear in the submitted article.

Declarations. Ethics approval and consent to participate consent for publication: Not applicable

Competing interests. The authors declare that they have no known competing financial interests or personal relationships that could have appeared to influence the work reported in this paper.

References

[1] C. P. Mark and S. Kamath, "Review of active space debris removal methods," *Space Policy* **47**, 194–206 (2019).
[2] K. Nagaoka, R. Kameoka and K. Yoshida, "Repeated impact-based capture of a spinning object by a dual-arm space robot," *Front Robot AI* **5**, 115 (2018).
[3] E. M. Botta, C. Miles and I. Sharf, "Simulation and tension control of a tether-actuated closing mechanism for net-based capture of space debris," *Acta Astronaut.* **174**, 347–358 (2020).
[4] M. Shan and L. Shi, "Post-capture control of a tumbling space debris via tether tension," *Acta Astronaut.* **180**, 317–327 (2021).
[5] W. Kuperberg, "Problems On Polytopes and Convex Sets," **In:** *DIMACS Workshop On Polytopes*, (1990) pp. 584–589.
[6] X. Li, Y. Qian, R. Li, X. Niu and H. Qiao, "Robust form-closure grasp planning for 4-pin gripper using learning-based attractive region in environment," *Neurocomputing* **384**, 268–281 (2020).
[7] W. G. Bircher, Whole-Hand Robotic Manipulation with Rolling, Sliding, and Caging Ph.D. thesis, Yale University ProQuest Dissertations & Theses, 2022. Available: https://www.proquest.com/openview/8cf2a932d38beab181b96225210a627e/1?pq-origsite=gscholar&cbl=18750&diss=y.
[8] J. C. Trinkle, J. M. Abel and R. P. Paul, "An investigation of frictionless enveloping grasping in the plane," *Int. J. Robotics Res.* **7**(3), 33–51 (1988).
[9] B. S. Eberman, Whole-Arm Manipulation: Kinematics and Control Ph.D. thesis, Massachusetts Institute of Technology, 1989. Available: http://refhub.elsevier.com/S0967-0661(18)30246-6/sb7.
[10] S. Makita and W. Wan, "A survey of robotic caging and its applications," *Adv. Robotics* **31**(19–20), 1071–1085 (2017).
[11] J. K. Salisbury, Whole-Arm Manipulation, **In:** *Proc. of the 4th Int. Symp. of Robotics Research*, Santa Cruz, CA, Cambridge MA: Published by the MIT Press, (1987) pp. 183–189.

https://doi.org/10.1017/S0263574725101938 Published online by Cambridge University Press

[12] J. Su, Z. Ou and H. Qiao, "Form-closure caging grasps of polygons with a parallel-jaw gripper," *Robotica* **33**(6), 1375–1392 (2015). doi: 10.1017/S0263574714000770.
[13] W. Yan, Z. Deng, J. Chen, H. Nie and J. Zhang, "Precision grasp planning for multi-finger hand to grasp unknown objects," *Robotica* **37**(8), 1415–1437 (2019). doi: 10.1017/S0263574719000031.
[14] M. Bamdad and M. M. Bahri, "Kinematics and manipulability analysis of a highly articulated soft robotic manipulator," *Robotica* **37**(5), 868–882 (2019). doi: 10.1017/S0263574718001376.
[15] E. Rimon and A. Blake, Caging 2d Bodies by 1-Parameter Two-fingered Gripping Systems, **In:** *Proceedings of IEEE International Conference on Robotics and Automation*, Vol. **2**, IEEE (1996) pp. 1458–1464.
[16] C. Agabiti, E. Ménager and E. Falotico, Whole-Arm Grasping Strategy for Soft Arms to Capture Space Debris, **In:** *2023 IEEE International Conference on Soft Robotics (RoboSoft)*, IEEE (2023) pp. 1–6.
[17] J. Zhang, Y. Hu, Y. Li, K. Ma, Y. Wei, J. Yang, Z. Wu, H. Rajabi, H. Peng and J. Wu, "Versatile like a seahorse tail: A bio-inspired programmable continuum robot for conformal grasping," *Adv Intell Syst.* **4**(11), 2200263 (2022).
[18] W. Wan, C. Sun, J. Yuan, X. Hou, Y. Guo, Y. Ou-yang, Q. Li, L. Zhao, H. Shi and D. Han, Adaptive Whole-Arm Grasping Approach of Tumbling Space Debris by Two Coordinated Hyper-redundant Manipulators, **In:** *Intelligent Robotics and Applications: 12th International Conference, ICIRA 2019*, Shenyang, China: Springer (2019) pp. 450–461, August 8-11, 2019, Proceedings, Part I 12
[19] D. Kim, Y. Maeda and S. Komiyama, "Caging-based grasping of deformable objects for geometry-based robotic manipulation," *ROBOMECH J.* **6**(1), 1–13 (2019).
[20] W. G. Bircher, A. S. Morgan and A. M. Dollar, "Complex manipulation with a simple robotic hand through contact breaking and caging," *Sci. Robot.* **6**(54), eabd2666 (2021).
[21] L. Beddow, H. Wurdemann and D. Kanoulas, A Caging Inspired Gripper Using Flexible Fingers and a Movable Palm, **In:** *2021 IEEE/RSJ International Conference on Intelligent Robots and Systems (IROS)*, IEEE (2021), pp. 7195–7200.
[22] N. Elangovan, L. Gerez, G. Gao and M. Liarokapis, "Improving robotic manipulation without sacrificing grasping efficiency: A multi-modal, adaptive gripper with reconfigurable finger bases," *IEEE Access* **9**, 83298–83308 (2021). doi: 10.1109/ACCESS.2021.3086802.
[23] T. Makapunyo, T. Phoka, P. Pipattanasomporn, N. Niparnan and A. Sudsang, Measurement Framework of Partial Cage Quality Based on Probabilistic Motion Planning, **In:** *2013 IEEE International Conference on Robotics and Automation*, IEEE (2013) pp. 1574–1579.
[24] S. Makita and K. Nagata, Evaluation of Finger Configuration for Partial Caging, **In:** *2015 IEEE International Conference on Robotics and Automation (ICRA)*, IEEE (2015) pp. 4897–4903.
[25] J. Y. W. Wan and C. Sun, The caging configuration design and optimization for planar moving objects using multi-fingered mechanism, *Adv. Robot*. **33**(18), 925–943 (2019).
[26] A. Shirizly, E. D. Rimon and W. Wan, "Contact space computation of two-finger gravity based caging grasps security measure," *IEEE Robot. Autom. Lett.* **6**(2), 572–579 (2020).
[27] A. Shirizly and E. D. Rimon, Computation and Selection of Secure Gravity Based Caging Grasps of Planar Objects, **In:** *2022 IEEE/RSJ International Conference on Intelligent Robots and Systems (IROS)*, IEEE (2022) pp. 1571–1578.
[28] R. R. Ma, W. G. Bircher and A. M. Dollar, Toward robust, whole-hand caging manipulation with underactuated hands, **In:** *2017 IEEE International Conference on Robotics and Automation (ICRA)*, IEEE (2017) pp. 1336–1342.
[29] W. G. Bircher and A. M. Dollar, DEsign Principles and Optimization of a Planar Underactuated Hand for Caging Grasps, **In:** *2019 International Conference on Robotics and Automation (ICRA)*, IEEE (2019) pp. 1608–1613.

Cite this article: Y. Zhou, Z. Jing, J. Huang, X. Dun, Y. Sun and K. Jiang (2025). "Configuration-based caging manipulation design for a cable-driven flexible arm with multi self-lockable links", Robotica **43**, 2693–2709. https://doi.org/10.1017/S0263574725101938

https://doi.org/10.1017/S0263574725101938 Published online by Cambridge University Press